



Multiscale modelling of CFRP composites exposed to thermo-mechanical loading from fire

Lei Wan^{a,b,*}, Scott L.J. Millen^{c,**}

^a School of Engineering, University of Hull, HU6 7RX, UK

^b Bristol Composites Institute, School of Civil, Aerospace and Mechanical Engineering (CAME), University of Bristol, University Walk, Bristol BS8 1TR, UK

^c School of Mechanical and Aerospace Engineering, Queen's University Belfast, Ashby Building, Belfast, BT9 5AH, Northern Ireland, UK

ARTICLE INFO

Keywords:

Polymer-matrix composites (PMCs)
Thermomechanical analysis
Representative volume element (RVE)
Modelling
Finite element analysis (FEA)

ABSTRACT

Carbon fibre reinforced polymers (CFRP) are prone to structural damage during extreme events such as fire. Typically, modelling the effect of fire on CFRP structures is carried out through mesoscale analysis to predict overall structural performance. In this study, Finite Element (FE) modelling has been conducted to investigate the effects of fire on CFRP specimens at both meso- and micro-scales. The mesoscale analysis informs the microscale analysis to examine the effects of fire on each constituent of the material. A comparison of thermal analysis at the meso- and micro-scales reveals less than a 6% difference in the predicted nodal temperature. For the first time, fire-induced progressive failure analysis has been conducted on the fibres, matrix, and fibre/matrix interface of representative plies within the composite laminates. Fibre breakage, matrix cracking, and interface debonding were accurately captured using representative volume element (RVE) models under thermo-mechanical loading, showing qualitatively excellent agreement with experimental data.

1. Introduction

In aerospace, automotive and maritime industries, composite materials such as carbon fibre reinforced polymers (CFRP) are becoming increasingly more common due to their beneficial material properties and lightweighting potential. However, composite materials are more susceptible to structural damage during extreme events such as low-velocity impact [1], lightning strikes [2] or fire [3,4], than traditional metallic structures.

Exposure to fire can have a detrimental effect on the structural performance of composites due to its adverse influences on the mechanical behaviour of the matrix. Generally, the onset of epoxy matrix thermal decomposition begins around 200–300 °C and is complete around 500–800 °C, while carbon fibres are thermally stable up to approximately 3000 °C [2]. As such, any fibre damage is more commonly attributed to the combined effects of mechanical and thermal loading [2]. During fire exposure, composite materials can release heat, smoke, and fumes [4]. Studies in the literature have focused on either the fire reaction properties or the structural fire behaviour of composites [5]. The former refers to a composite's time-to-ignition, flame spread, and heat release rate characteristics which are well documented and comprehensively described [6–8]. However, the latter considers the structural performance characteristics such as stiffness, strength, and fatigue life of

a composite, which declines when subjected to fire, increasing the likelihood of material failure through buckling or collapse.

The effect of fire on composites has been assessed using both experimental [9,10] and simulation approaches. A significant number of studies have attempted to capture and represent the behaviour of composite materials exposed to fire to provide information on the effects on stiffness and strength, mechanical integrity and burn-through resistance [4,11–18]. Fire-induced damage modes of composite materials have been characterised as matrix cracking, delamination, char formation, fibre fracture, and blowout [19]. The traditional approach used to assess the structural reaction of composite materials to fire has entailed empirical investigations, wherein structures are exposed to loading conditions mirroring real-world scenarios [18]. Although such experimentation yields indispensable insights, its execution is both financially burdensome and challenging to regulate. Consequently, the imperative to develop robust fire analysis models becomes readily apparent [4].

Modelling of composite structures has progressed significantly in recent years with models at different fidelities and length scales. Multiscale modelling, combining or linking models across length scales, is a very useful method for composite materials with hierarchical features, and many challenging studies are being conducted. For example, studies have completed micro/mesoscale fracture modelling

* Corresponding author at: School of Engineering, University of Hull, HU6 7RX, UK.

** Corresponding author.

E-mail addresses: L.Wan@hull.ac.uk (L. Wan), scott.millen@qub.ac.uk (S.L.J. Millen).

[20,21], modelling of deformation/fracture from molecular scale to micro/mesoscale simulations [22–24], modelling of cure-induced deformation incorporating heat conduction equations, viscoelastic constitutive laws, and curing reactions [25], and multiscale modelling by Direct FE2 methods [26,27]. By far the most popular modelling approach is the mesoscale model in which each ply is modelled as a single unit with interaction properties, such as surface-to-surface contact, included between neighbouring plies [4,14]. Other works have modelled the effect of fire on sandwich panels and found primary failure as delamination at the facesheet/core interface [12,28]. Literature studies have also investigated the effect of the ply stacking sequence [19] and thickness [13] on composite fire resistance. Although mesoscale models have been used to investigate the overarching structural dynamics, microscale models offer the capability to differentiate damage mechanisms inherent to each constituent component, namely fibres, matrix, and the fibre/matrix interface. This microscale approach provides a deeper understanding of heat transfer phenomena and fire dynamics within and between constituent materials.

Micromechanics-based RVE models have proven to be an effective computational tool to perform a progressive failure analysis of unidirectional composites under multiaxial loading conditions [29–32]. RVE models take into account the geometry and spatial distributions of the fibres, and the mechanical properties of the constituents, which should be large enough to be representative of the macroscale materials while small enough to maintain the computational cost. Microscopic or representative volume element (RVE)-based modelling, using a small representative volume to represent the realistic material, even with manufacturing-induced defects [33], is typically used to characterise the macroscopic response of composites. RVE modelling has also been used in multi-scale modelling of unidirectional composites (UD) [34]. Typically, RVE models have used an average fibre diameter $d_f = 7 \mu\text{m}$ and fibre volume fraction $V_f = 60\%$, measuring $50 \mu\text{m} \times 50 \mu\text{m} \times 10 \mu\text{m}$ [29–31]. Parallel fibres have been randomly distributed using random sequential adsorption (RSA) algorithms [35]. Recently, Wan et al. [29,30] constructed a failure criterion for IM7/8552 UD composites under biaxial loading using artificial neural network (ANN) models, based on computational micromechanical modelling, considering the probability of failure. Data-driven failure predictions were conducted based on representative failure points in each biaxial loading case and were extended by machine learning techniques considering the probability of failure.

In the failure analysis of composite materials using RVE modelling, periodic boundary conditions are usually used to maintain the periodicity of stress and displacement fields. However, it has also been reported in [36,37] that for sufficiently large RVEs with more than 30 fibres embedded in the matrix [29,35], the results obtained from the periodic boundary conditions were close to those obtained from displacement or traction boundary conditions. Recently, Millen and Lee [38] completed three-dimensional (3D) finite element (FE) simulations to study the effects of lightning strikes on the microscale behaviour of CFRP. This approach provided better understanding of lightning-induced thermo-mechanical damage at a fundamental level. Thermo-mechanical damage was predicted using a ductile plasticity model with Drucker–Prager yield criterion for epoxy matrix failure, and cohesive surfaces for fibre-matrix interface debonding. However, an understanding of the effect of fire on the microscale behaviour of CFRP is not well established.

1.1. Summary

The literature has shown that finite element modelling can be used to predict both damage resulting from fire and residual strength post-fire [13]. In order to predict composite failure more accurately, it becomes important to understand and model the behaviour of composite materials in a realistic loading scenario to obtain reliable safety data for future designs. Existing fire simulation research has largely focused

on a singular modelling strategy - mesoscale models, either monolithic or sandwich panels, with a constant flux loading applied to a finite area on the front face. While these mesoscale models have been used to study overall structural behaviour, RVE-based micro-scale models can characterise unique damage mechanisms of each constituent at a smaller length scale.

Therefore, the work in this paper focuses on multiscale modelling of CFRP composites exposed to thermo-mechanical loading, specifically representative of fire. A mesoscale model is developed and validated against the established experimental literature. Predictions from this mesoscale model inform the thermal, loading, and boundary conditions on the RVEs for the progressive failure analysis of CFRP constituents (fibre, matrix and the fibre/matrix interface) during thermo-mechanical loading.

2. Multiscale macro–microscale modelling strategy

2.1. Mesoscale modelling of CFRP composite laminates

2.1.1. Heat transfer modelling

The mesoscale model of the quasi-isotropic AS4/3501-6 carbon fibre-epoxy composite [+45/90/−45/0]_s is outlined in Fig. 1a and b. This model was derived from the experimental work of Grigoriou and Mouritz [39]. Fig. 1a shows the dimensions and FE mesh used in the mesoscale model, which measured 600 mm × 50 mm × 6.4 mm with a typical ply thickness of 0.15 mm [39]. A heat flux load of 50 kW/m² was applied to a 100 mm long section of the front face of the specimen, as shown in Fig. 1b, in line with the experimental arrangement [39]. DC3D8 8-node linear brick solid heat transfer elements were used within heat transfer simulations.

The governing equation for heat conduction in this simulation is expressed as follows:

$$\rho C_p \frac{\partial T}{\partial t} = \nabla \cdot (k \nabla T) = \frac{\partial}{\partial x} \left(k_x \frac{\partial T}{\partial x} \right) + \frac{\partial}{\partial y} \left(k_y \frac{\partial T}{\partial y} \right) + \frac{\partial}{\partial z} \left(k_z \frac{\partial T}{\partial z} \right) + q_v \quad (1)$$

where T is temperature (°C), t is time (s), k is thermal conductivity of the material (W/m K), ρ is density (kg/m³), q_v is the rate of energy generated per unit volume (W/m³) and C_p is the specific heat capacity (J/kg K).

Table 1 shows the temperature-dependent material properties used for AS4/3501-6 carbon/epoxy composite [40]. The epoxy matrix in CFRP degrades and decomposes in the temperature range of 300–800 °C. As the matrix begins to decompose, a region of shiny resin, with matrix cracking and delamination is produced. Further, more severe damage, corresponding to the end of matrix decomposition is likely to be deeper with char residue and fibre fracture. Carbon fibres were assumed to ablate above 3316 °C, the fibre sublimation temperature, and at 3334 °C the fibres have reached a pure carbon/char state.

A predefined field was used to assign an ambient temperature of 25 °C at the start of the simulation. The change in material behaviour is accounted for by the temperature dependent material properties in Table 1 but also by ABAQUS user-subroutines. HETVAL and USDFLD were used to define the thermal behaviour of the material. HETVAL determined the extent of matrix thermal decomposition at each time increment, accounting for decomposition kinetics and internal heat generation, while the material properties were updated using USDFLD [5]. While the values in Table 1 are listed at discrete points, these are assumed to change linearly with increasing temperature. In addition, matrix decomposition is assumed to vary linearly between onset and complete decomposition.

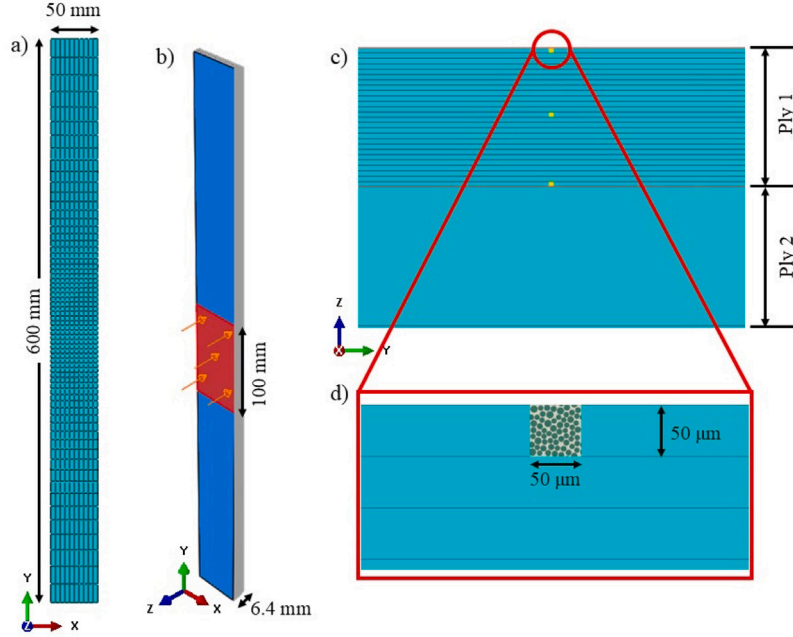


Fig. 1. Mesoscale model setup and conversion to microscale RVE model.

Table 1
AS4/3501-6 carbon/epoxy thermal material properties [40].

Temperature (°C)	Density (kg/m ³)	Specific heat (J/kg °C)	Thermal conductivity		
			Fibre (W/m K)	Transverse (W/m K)	Through-thickness (W/m K)
25	1520	1065	46.6	0.68	0.68
350	1520	2100	24.7	0.37	0.37
510	1100	2100	14.6	0.18	0.18
1000	1100	5750	11.7	0.13	0.13
3316	1100	5785	0.10	0.10	0.10
3334	1100	5875	0.10	0.10	0.10
Temperature range (°C)			Energy released (J)		
Resin decomposition		300–800	4.8 × 10 ⁶		
Fibre ablation		3316–3334	43 × 10 ⁶		

2.1.2. Thermo-mechanical modelling

Thermo-mechanical analysis was completed in Abaqus/Explicit using a dynamic, temperature–displacement, explicit analysis with C3D8RT elements (8-node trilinear displacement and temperature, reduced integration with default hourglass control). This step could predict mechanical damage due to the combined effects of mechanical and thermal strains. Intralaminar damage was captured using a VUMAT material model developed previously [41].

A combination of Hashin, for fibre direction tension and compression and transverse tension, and Puck failure initiation criteria, for transverse compressive and through-thickness directions, were used, as shown in Eqs. (2)–(4).

$$F = \begin{cases} \left(\frac{\sigma_{11}}{X_T} \right)^2 + \left(\frac{\sigma_{12} + \sigma_{13}}{S_{12}} \right)^2, & \sigma_{11} \geq 0 \\ \left(\frac{\sigma_{11}}{X_C} \right)^2, & \sigma_{11} < 0 \end{cases} \quad (2)$$

$$F = \begin{cases} \left(\frac{\sigma_{22}}{Y_T} \right)^2 + \left(\frac{\sigma_{12}}{S_{12}} \right)^2 + \left(\frac{\sigma_{13}}{S_{12}} \right)^2, & \sigma_{22} \geq 0 \\ \left(\frac{\sigma_{33}}{Y_T} \right)^2 + \left(\frac{\sigma_{13}}{S_{12}} \right)^2 + \left(\frac{\sigma_{23}}{S_{12}} \right)^2, & \sigma_{22} < 0 \end{cases} \quad (3)$$

$$F = \left(\frac{\sigma_{11}}{X_T} \right)^2 + \left(\frac{\sigma_{33}^2}{Y_T + Y_C} \right) + \left(\frac{\sigma_{23}}{S_{12}} \right)^2 + \left(\frac{\sigma_{33}}{Y_T + Y_C} \right) \quad (4)$$

A linear damage evolution law was defined after damage initiation. Strain rate effects were included by scaling E_2 , E_3 and the intralaminar

strength and fracture toughness, based on the observed strain rate regime (quasi-static, intermediate, or high). Heating rate effects offset the temperature at which the moduli and strength of the material reduced [41].

The predicted temperature profile from the heat transfer analysis was transferred to the thermo-mechanical analysis using Python scripts and a well-established methodology, not explained here for brevity but available in Refs. [2,41].

Delamination between neighbouring plies was captured using cohesive surfaces with a bi-linear traction-separation law [41]. The onset of interfacial damage was governed by the quadratic stress criterion and the dissipation of the fracture energy during the propagation of the damage was governed by the Benzeggagh and Kenane (B-K) criterion [42]:

$$G^C = G_n^C + (G_s^C - G_n^C) \left(\frac{G_s + G_t}{G_n + G_s + G_t} \right)^{\eta_{BK}^C} \quad (5)$$

The temperature-dependent elastic mechanical properties of the AS4/3501-6 carbon/epoxy composite are shown in Table 2, and the intralaminar and interlaminar strengths and fracture energies can be found in Table 3.

Since the RVE model measured $50 \mu\text{m} \times 50 \mu\text{m} \times 50 \mu\text{m}$ with fibre diameters of $5.3\text{--}7 \mu\text{m}$ [31], it was necessary to discretise the mesoscale models in the areas of interest. Therefore, the front and rear plies of the mesoscale model had twenty-six elements through the thickness,

Table 2
The elastic mechanical properties of AS4/3501-6 carbon/epoxy composites.

Temperature (°C)	E_1 (MPa)	$E_2 = E_3$ (MPa)	$G_{12} = G_{13}$ (MPa)	G_{23} (MPa)	$\nu_{12} = \nu_{13}$	ν_{23}	$\alpha_{11} \times 10^{-8}$	$\alpha_{22} = \alpha_{33} \times 10^{-5}$
25	137 000	8200	4360	3000	0.32	0.44	1.8	2.16
200	137 000	6560	3488	2400	0.32	0.44	5.4	3.78
260	137 000	82	34.88	24	0.32	0.44	5.4	3.78
600	137 000	4.1	1.744	1.2	0.32	0.44	5.4	3.78
3316	137 000	4.1	1.744	1.2	0.32	0.44	5.4	3.78
>3316	1370	0.41	0.1744	0.12	0.32	0.44	5.4	3.78

Table 3
The strengths of AS4/3501-6 carbon/epoxy composites and interlaminar interface properties [43].

Intralaminar strength and fracture toughness					Interlaminar interface properties			
X_t (MPa)	X_c (MPa)	Y_t (MPa)	Y_c (MPa)	$S_{12} = S_{13} = S_{23}$ (MPa)	t_n^0 (MPa)	$t_s^0 = t_t^0$ (MPa)	G_n^C (kJ/m ²)	$G_s^C = G_t^C$ (kJ/m ²)
2280	1440	57	228	71	20	34	0.32	2.0

giving an approximate element thickness of 50 μm . Three RVE models were created for the plies of interest (i.e. 45°, 90° and 0° plies) at the 1st, 13th and 26th elements, of these plies, as shown in yellow on ply one in Fig. 1c. The corresponding RVE representation is shown within the element of this ply in Fig. 1d. This arrangement allowed the flux loading and temperature at three distinct points within the front and rear plies to be extracted for use within and for verification of the microscale model.

In the mesoscale model, the in-plane mesh was refined around the loading area to a size of 2.5 mm \times 2.5 mm increasing to 2.5 mm \times 20 mm at the ends of the specimen, using biasing. As a result, standard plies had 1720 elements while the plies of interest, suitable for data transfer to the RVE models, had 17,160 elements each.

2.2. Microscale modelling

2.2.1. FE model set-up

In this study, the microstructure of the RVEs was generated using combined experimental data and an initial periodic shaking model using a discrete element method [44], resulting in a fibre volume fraction of 60% and average fibre diameters between 5.3–7 μm . It was found that the depth of RVE models had insignificant influence on the prediction of mechanical properties [45]. Therefore, to capture the deformation and failure of the matrix and fibre/matrix interface due to the different thermal expansion coefficients between the three constituents, a depth of 50 μm was selected. With respect to fibre failure under longitudinal tension, the length of the RVE model was found to have a significant influence on longitudinal properties and 300 μm was concluded to be enough to capture fibre failure [46]. Therefore, the final 3D RVE models were created by extruding the 2D geometrical model along the fibre direction by 50 μm and 300 μm to capture the matrix and fibre/matrix interface dominated failure and fibre dominated failure, respectively, as shown by RVE1 and RVE2 in Fig. 2.

For microscale heat transfer modelling, 8-node linear brick and 6-node linear triangular prism solid heat transfer elements (DC3D8 and DC3D6) were used to mesh fibres, matrix and fibre/matrix interface, with the incident heat flux calculated from mesoscale simulations. In total, 50,616 and 487,000 elements were used to mesh RVE1 and RVE2 models, respectively. The predicted temperature distribution from the RVE heat transfer simulation was loaded as a predefined temperature field for the thermo-mechanical failure analysis.

For thermo-mechanical failure analysis, the fibres and matrix in the RVE models were discretised with hexahedral solid elements (C3D8R), with a reduced integration scheme, and wedge elements (C3D6R), while the interface is meshed with 8-node cohesive elements (COH3D8), see Fig. 2. The total of 50,616 and 487,000 elements are utilised to better capture the stress distribution between neighbouring fibres and

to balance model accuracy and computational cost. Mass scaling was employed to accelerate the numerical simulations with a stable time increment of 5×10^{-6} s. More details on the RVE modelling can be found in [29–31].

2.2.2. Constitutive model of constituents

The carbon fibre was modelled as a brittle linearly elastic and transversely isotropic solid. A thermo-dynamically consistent isotropic damage model was used to define the fibre damage, which can only be activated by the longitudinal tensile stress. The damage activation function, also known as the damage initiation index, reads:

$$D_f = \frac{\sigma_{11}}{X_f^t} \quad (6)$$

where σ_{11} is the applied longitudinal tensile stress and X_f^t is the longitudinal tensile strength of the fibre. In order to capture the intrinsic stochastic (i.e. flaw-dominated) nature in the longitudinal tensile strength of carbon fibres [47], the two-parameter Weibull distribution function [48] is commonly used. However, it has been shown that the Weibull distribution is not the best suited for carbon and glass fibres [49,50], thus, the Power-Law Accelerated Weibull (PLAW) distribution [49] was proposed based on the Weibull distribution:

$$P(\sigma) = 1 - \exp\left[-\left(\frac{L}{L_0}\right)^\alpha \left(\frac{\sigma}{\sigma_0}\right)^{m_0}\right] \quad (7)$$

where P represents the failure probability at the applied stress σ , and σ_0 and m_0 are the scale and shape parameters of the Weibull function, respectively. L_0 and L are the reference and gauge length of the specimen, respectively. The additional exponent α controls the influence of the element length on the failure probability. Then, the element-wise failure probability associated tensile strength X_i^t can be obtained with transformation of the above equation and the generation of a random scalar P_i in the interval [0,1] for the i th element:

$$X_i^t = \sigma_0 \left[-\left(\frac{L}{L_0}\right)^\alpha \ln(1 - P_i) \right]^{\frac{1}{m_0}} \quad (8)$$

A linear softening law was used to model the damage propagation of fibres. The damage variable for longitudinal tensile failure is given by:

$$d_f = \frac{\delta_{eq}^f (\delta_{eq}^f - \delta_{eq}^0)}{\delta_{eq}^f (\delta_{eq}^f - \delta_{eq}^0)} \quad (9)$$

where δ_{eq}^f is the equivalent displacement after damage initiation, δ_{eq}^0 is the equivalent displacement at which the damage initiation criterion is satisfied ($D_f = 1$), and δ_{eq}^f is the equivalent displacement at which the material is failed ($d_f = 1$).

To avoid mesh-dependent damage localisation, the softening response after damage initiation was characterised by a stress–displacement response rather than a stress–strain response. The crack

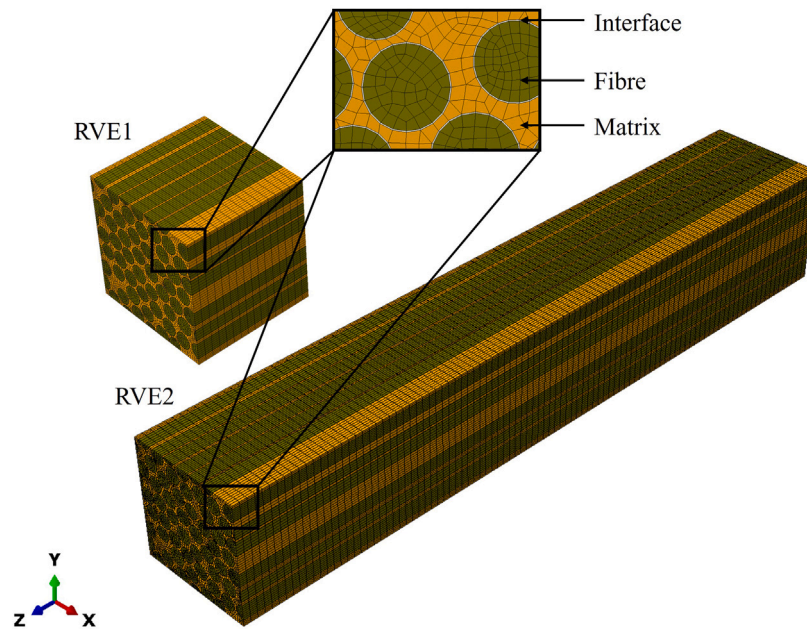


Fig. 2. Three constituents based RVE models for matrix and interface dominant failure (RVE1) and fibre dominant failure (RVE2).

Table 4
AS4 carbon fibre properties [49].

Constituent	σ_0 (MPa)	L_0 (mm)	α	m_0	G_f (N/mm)
AS4 fibre	4275	12.7	0.6	8	0.05

band model [51] was implemented to regularise the dissipated fracture energy:

$$\delta_{eq}^f = \frac{2G_f}{X_i^f} \quad (10)$$

A VUMAT subroutine was developed to predict the progressive failure process of a single AS4 carbon fibre and then used for the stochastic failure prediction of fibres in a 0° unidirectional composite in ABAQUS/Explicit. The PLAW-related parameters for AS4 carbon fibre are found in Table 4. It is important to note that the experimental reproduction of the fibre failure within unidirectional composites under longitudinal tension could be significantly improved with the consideration of probabilistic failure behaviour of fibres (i.e. Weibull distribution of fibre strength [48]) and the preferential fracture tendency of adjacent fibres determined by the fibre/matrix combination [52] and the resulting clustering of fibre fractures [52,53]. The consideration of aforementioned factors on fibre failure prediction under combustion is out of the scope of the current work, thus only the Weibull distribution of fibre strength is considered in the current work.

Carbon fibres, like CFRP plies and laminates, can exhibit anisotropic elastic moduli and thermal conductivity and thermal expansion due to their molecular structure [54,55]. Therefore, it is necessary to take the anisotropic thermal and elastic properties of fibres into account as it could influence local temperature distributions and degradation behaviours. However, it should be noted that in the current study, such influence could be limited since the matrix and interface fail early under transverse tension and decompose at much lower temperatures, also observed previously [38]. In addition, the difference in directional thermal properties matters most in the longitudinal tension direction when considering anisotropy, where mechanical loading plays a vital role. Carbon fibres are thermally stable up to approximately 3000°C , while the peak temperatures in the studies herein are around $600\text{--}700^\circ\text{C}$. Therefore, anisotropic thermal conductivity of fibres should have limited influence on the final qualitative result under thermo-mechanical loading.

Table 5
Thermal material properties of constituents [55,56].

Constituent	Density (kg/m^3)	Specific heat ($\text{J}/\text{kg } ^\circ\text{C}$)	Thermal conductivity	
			Longitudinal ($\text{W}/\text{m K}$)	Transverse ($\text{W}/\text{m K}$)
Carbon fibre (AS4)	1500	1065	6.9	2.4
Epoxy (3501-6)	1265	1065	0.5	0.5
Interface	1265	1065	0.5	0.5

The polymeric matrix was assumed to be an isotropic elastoplastic solid. Temperature-dependent matrix properties, including Young's modulus, Poisson's ratio and coefficients of thermal expansion, were calculated from an experimentally fitted quadratic polynomial [56]. The extended linear Drucker–Prager yield criterion together with a ductile damage criterion, available in ABAQUS/Explicit [57], was used to capture brittle failure under tension and plastic deformation under compression/shear. After the onset of damage, the propagation of damage was governed by a damage evolution law, characterised by the critical fracture energy of the polymer. The characteristic length of elements was adopted to alleviate the mesh dependency of the numerical results. The fracture strain in the Ductile damage criterion was calibrated for different temperatures in the one-element calibration process. Further details of this constitutive model and of the numerical implementation can be found in Refs. [29].

The interface bonding between the fibres and the matrix was modelled using cohesive elements with a bilinear traction separation law. Following linear elasticity, the damage onset was governed by a quadratic stress interaction criterion, while propagation was controlled by the energy-based Benzeggagh-Kenane damage criterion [42], considering the fracture mode-dependent energy dissipation. At room temperature, the interface fracture energy in mode I, G_{IC} , is extremely difficult to measure experimentally, so a relatively small value of $2 \text{ J}/\text{m}^2$ was used in this study, which has been proven reasonable [29,30]. Furthermore, due to the absence of experimental data, the fracture energy for the shear modes was assumed to be equal to $95 \text{ J}/\text{m}^2$ [58], which is the experimentally measured fracture energy of epoxy 3501-6. At 600°C the material properties are assumed to be 1/100 of the room temperature properties. The thermal material properties of the fibre, matrix and fibre/matrix interface can be found in Tables 5–8.

Table 6
Temperature dependent mechanical properties of constituents [46,56].

Temperature (°C)	Carbon fibre AS4						Epoxy 3051-6	
	E_1 (MPa)	$E_2 = E_3$ (MPa)	$G_{12} = G_{13}$ (MPa)	G_{23} (MPa)	$\nu_{12} = \nu_{13}$	ν_{23}	E (MPa)	ν
25	225 000	15 000	15 000	15 000	0.2	0.48	4315	0.38
100	225 000	15 000	15 000	15 000	0.2	0.48	3600	0.38
200	225 000	15 000	15 000	15 000	0.2	0.48	2458	0.39
260	225 000	15 000	15 000	15 000	0.2	0.48	1821	0.39
600	225 000	15 000	15 000	15 000	0.2	0.48	18.21	0.40

Table 7
Thermal expansion material properties of constituents [38,56].

Temperature (°C)	Carbon fibre AS4		Epoxy 3051-6	Interface
	α_{11} ($\times 10^{-8}$)	$\alpha_{22} = \alpha_{33}$ ($\times 10^{-5}$)	α ($\times 10^{-5}$)	α ($\times 10^{-5}$)
25	1.80	4.14	4.14	4.14
200	5.40	6.25	6.25	6.25
260	5.40	7.02	7.02	7.02
600	5.40	11.18	11.18	11.18
3316	5.40	44.42	44.42	44.42

Table 8
Temperature dependent mechanical properties of fibre/matrix interface [30,58].

Temperature (°C)	$K_n = K_s = K_t$ (MPa/mm)	r_n^0 (MPa)	$r_s^0 = r_t^0$ (MPa)	G_{IC} (J/m ²)	$G_{IIC} = G_{IIIC}$ (J/m ²)
25	10 ⁷	60	92	2	95
600	100 000	0.6	0.92	0.02	0.95

2.2.3. Loading and boundary conditions

In the one-way meso- to microscale coupled framework, the resultant heat flux was obtained at designated nodes in 45°, 90° and 0° plies from mesoscale simulations. These heat flux loads were applied to the top surface of the RVE models perpendicular to the Y coordinate, see Fig. 2. The heat transfer simulations of different plies were performed using ABAQUS/Standard with a total time of 1600 s. The predicted temperature profile in the RVE, obtained from the heat transfer simulation, was then used as a predefined temperature field in the thermo-mechanical failure analysis. As mentioned previously, sufficiently large RVEs do not require periodic boundary conditions. Rather, displacement or traction boundary conditions can be used. Thus, in this study, resultant uniform displacements at the elements in the centre region of the mesoscale simulations were loaded onto the surface nodes of each RVE.

2.2.4. Validation of constitutive models of constituents

Progressive failure analysis was conducted on a single AS4 carbon fibre to validate the constitutive model and the experimentally determined PLAW parameters [49]. In the FE model, the radius of the AS4 fibre was 3.5 μm while the length of the fibre was 200 μm . In total, 5610 C3D8R elements were used for the discretisation of the model, in which the strength of each element followed the PLAW distribution, see Fig. 3(a). Manufacturing-induced defects on the surface of carbon fibre were accounted for by the randomly assigned small strength at the outer surface, represented by the blue element at the cross-section A-A with a comparison of the scanning electron microscopy (SEM) image [59]. Small 3-element wide regions at opposite ends of the fibre were assumed to be elastic to avoid edge effects. Displacements were applied on the nodes on both sides until the fibre failed. Fig. 3(b) shows the nonlinear stress–strain curve of the single AS4 carbon fibre under longitudinal tension. The final failure strength of the fibre was 4430 MPa, with a 1.6% difference compared to the experimental data 4501 MPa from the HEXCEL product data sheet for HexTow[®] AS4 carbon fibre [60]. At the strain ϵ_1 , damage initiated from the weakest region with the smallest strength at the centre when the damage initiation index $D_f = 1$, followed by other isolated weak regions when the strain increased to ϵ_2 and ϵ_3 . Fig. 3(c) shows the damage initiation contour

at different strains. The propagation of damage from ϵ_2 can be seen in Fig. 3(d) at the same locations where damage occurred. The damage propagated towards both sides and finally failed when the damage variable $d_f = 1$ in the centre.

The parameters in the Drucker–Prager yielding criterion for epoxy 3501-6 were calculated at room temperature and were assumed to be temperature independent due to the lack of experimental data. The hardening of the material was defined with uniaxial tensile yielding stress at 25 °C and 150 °C. The fracture strain in the Ductile damage criterion at both temperatures was calibrated from the experimental data [61] based on the one-element FE simulations. The FE model of the element and the loading and boundary conditions can be found in Fig. 4. It can be seen that there is good agreement between the experimental data and the numerical prediction with the calibrated fracture strain.

3. Results and discussions

3.1. Mesoscale modelling results

Fig. 5 compares the temperature–time profiles measured at the front and rear surfaces of the experimental and mesoscale simulation specimens when exposed to the thermal flux of 50 kW/m². There is generally good agreement between the simulation and the experiment with some slight variation in the predictions. For example, the predicted peak temperature at the front face was 11% lower than the experiment at the end of the simulation; however, the general trends of temperature on both front and back faces were captured.

The temperature and flux values were extracted from the model using the output variables NT11 and HFL, respectively. Fig. 6 shows the variation in predicted temperature and flux at the central nodes at the top, middle and bottom surfaces of the ply one. It can be seen that the variation in both measures is small across the thickness of the single ply, varying by around 6 °C or less than 1%.

Fig. 7 shows the heated surface and through-thickness thermal damage profiles after flux loading of 50 kW/m². The moderate damage area (areas where 300 °C $\leq T < 500$ °C) was 6050 mm² and extended through the entire specimen thickness. The severe damage area (areas where $T \geq 500$ °C) was 4500 mm² and extended twenty-three plies deep or 3.1 mm.

Fig. 8 compares the X-ray computed tomography image of a through-thickness section of the composite and the corresponding model prediction of delamination following exposure to the heat flux of 50 kW/m² for 1000 s. The predicted delamination area and depth were 10,900 mm² and twenty-three plies (3.1 mm), respectively. The delamination area was 80% higher than the moderate thermal damage area.

3.2. Thermal analysis at the microscale

3.2.1. The effect of fibre distribution

The microscale temperature distribution at the mid-point of the top layer of the composite laminate (45° ply) was predicted using RVE models considering different potential fibre distributions and data from the 13th element of the mesoscale model.

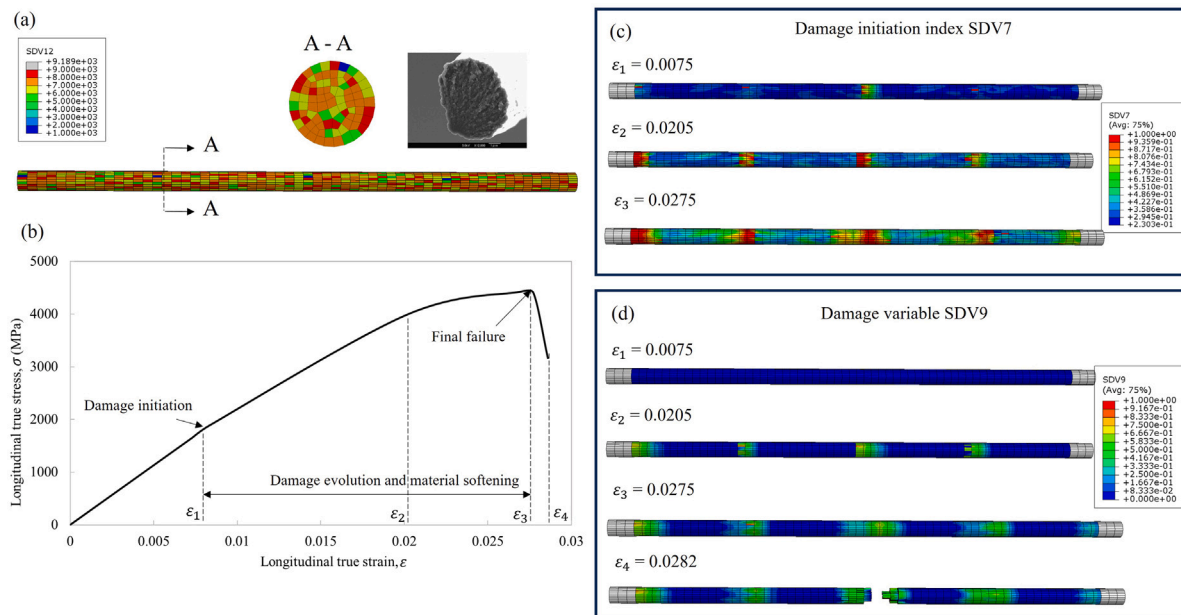


Fig. 3. (a) Element-wise PLAW distribution of fibre strengths and cross-section comparison with experimental SEM image [59]; (b) Predicted stress-strain curve of a single fibre with strength distribution from (a) longitudinal tension; (c) Damage initiation contour at different strains; (d) Damage progression at different strains.

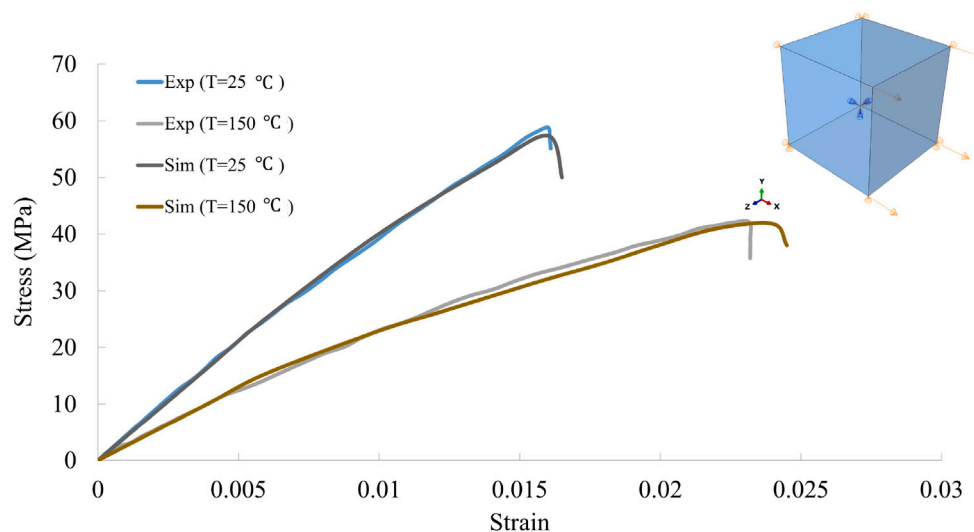


Fig. 4. Comparison of stress-strain curves of epoxy 3501-6 under uniaxial tension at 25 °C and 150 °C between experiments [61] and one-element FE simulations.

The resultant thermal flux of 48 kW/m² at the top node of the 13th element from the mesoscale simulation was applied to the top surface of the RVE model. The influence of microstructure on the temperature prediction was investigated by taking into account of four different randomly distributed fibre distributions. Fig. 9 shows the comparison of predicted node temperature fields with different fibre distributions at the middle of the top layer. Due to the differences in conductivity of the fibres and the matrix, an obvious margin between different temperature intervals can be observed. The predicted maximum temperature ranges from 682.1 to 685.1 °C, indicating insignificant influences from the fibre distribution. When comparing the predicted temperatures in both microscale and mesoscale models, there was an average difference of 5.8% between the length scales.

3.2.2. The effect of fibre orientation

The layers of interest (i.e. 45° 90° and 0° plies) were discretized with 26 elements in the thickness direction of the mesoscale models. To compare predicted node temperatures at different length scales, three

locations, 1st, 13th and 26th elements, in the 90° and 0° plies close to the top layer were selected to compute the temperature within the RVE models. The resultant heat flux from the mesoscale simulation was used as a loading condition in the RVE models. Table 9 compares the predicted temperature from both length scales at different elements. The temperatures in the mesoscale and microscale models were within 6%, which shows an excellent agreement.

3.3. Microscale progressive failure analysis of CFRP composites exposed to thermo-mechanical loading

This section highlights the progressive failure analysis of the different plies along thickness directions under thermo-mechanical loading conditions. Fig. 10 shows the transverse and longitudinal stress-temperature curves of the RVE in the centre of the top layer 45° and neighbouring 90°, and 0° plies following the thermo-mechanical loading and boundary conditions obtained from mesoscale simulations, respectively. The same RVE model was used to represent the

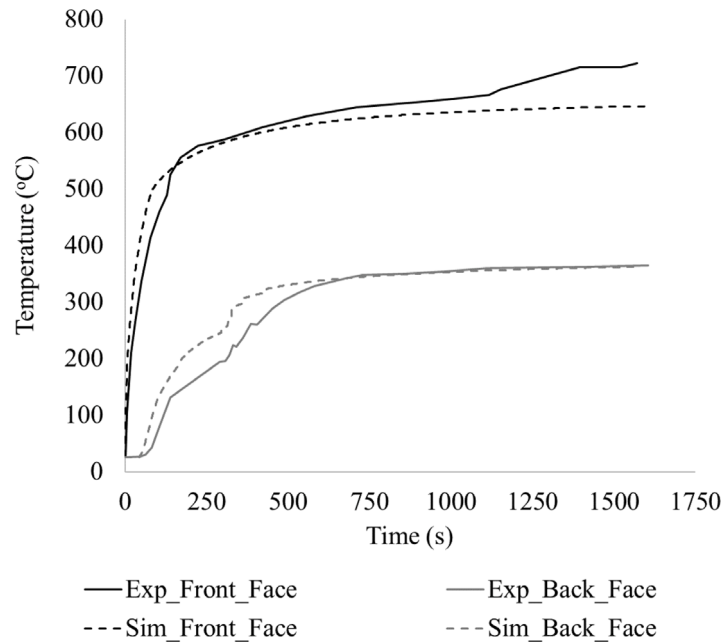


Fig. 5. Temperature-time profiles measured at the front and rear surfaces of the experimental and mesoscale simulations specimens when exposed to the thermal flux of 50 kW/m².

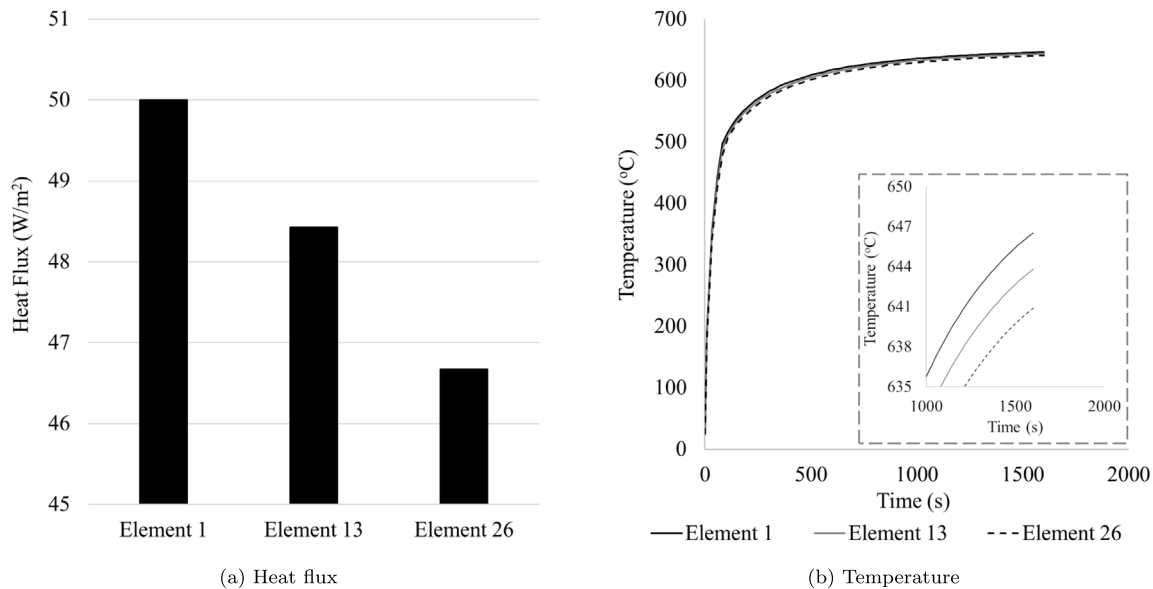


Fig. 6. Predicted (a) heat flux and (b) temperature at each of the three central elements through the thickness of the front ply.

Table 9
Comparison between predicted mesoscale node temperature and microscale homogenised temperature at different locations of 90° and 0° plies.

Scale & Ply	Element 1 (°C)	Element 13 (°C)	Element 26 (°C)
Mesoscale 90° ply	639.4	636.3	633.6
Microscale 90° ply	630.4	622.2	613.8
Difference	1.4%	2.2%	3.1%
Mesoscale 0° ply	625.3	622.7	619.7
Microscale 0° ply	600.6	591.7	582.6
Difference	3.9%	4.9%	5.9%

microstructure of the top layer 45° and the middle 90° layers, while the thermo-mechanical loading and boundary conditions were calculated from the mesoscale simulation. Details of the damage initiation

and propagation of each constituent including fibres, matrix and fibre/matrix interface until final failure are well captured in Figs. 11–15, with qualitative comparison with experimental SEM images. Analysis of damage modes during thermo-mechanical loading illustrates a process of damage progression in the composite, at the microscale, broadly captured by four temperature boundaries.

Initially, the specimen and therefore microscale model were at room temperature. As thermal loading was applied to the 45° ply, the temperature increased. At 50 °C fibre/matrix interface damage initiated at the edges of the RVE under transverse tension, as shown in Fig. 11. Further heating produced significant debonding of the interface when the temperature reached 154 °C. Matrix damage initiation occurred around 175 °C, resulting in the loss of load-carry capacity. This is shown by the peak stress (blue line) for the 45° ply shown in Fig. 10.

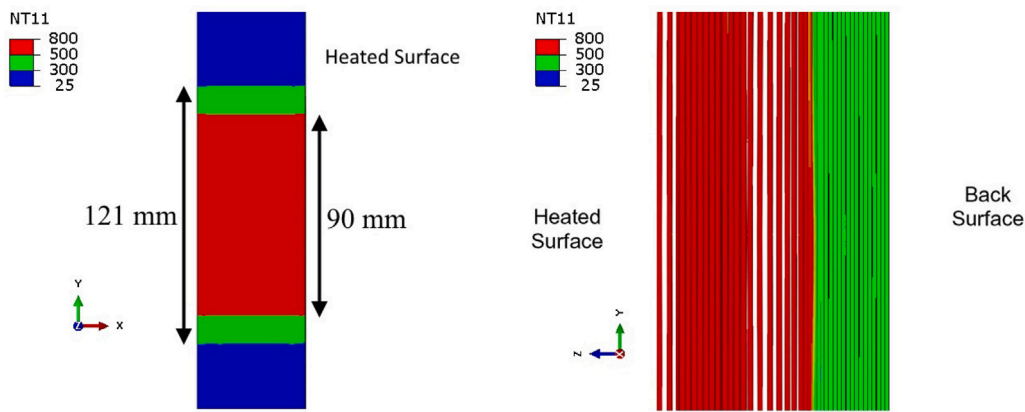


Fig. 7. Moderate and severe thermal damage contours at (a) heated surface and (b) through the specimen thickness.

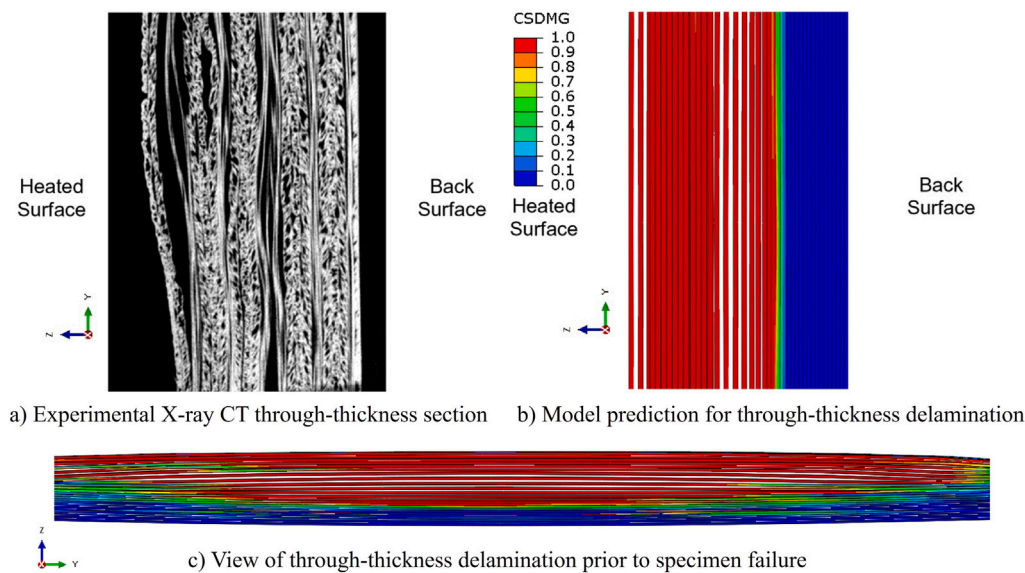


Fig. 8. Comparison of X-ray computed tomography image of a through-thickness section of the composite and the corresponding model prediction of delamination following exposure to the heat flux of 50 kW/m² for 1000 s.

Critical damage occurred in the matrix at 200 °C with isolated failure events.

Matrix cracking and fibre/matrix interface debonding of the 45° ply under thermo-mechanical loading was well captured, with good qualitative agreement with the SEM images of the top layer 45° ply [62]. Unlike the progressive failure events of the matrix in the top layer 45° ply, the damage to the matrix in the neighbouring 90° layer started to initiate at 154 °C, shown in Fig. 13 which may be due to the different resultant displacements obtained from the mesoscale simulation.

Earlier damage events in the matrix of the RVE of the 90° layer led to a smaller predicted homogenised stress, compared to the predicted stress of the top layer 45° ply, see Fig. 10. The predicted failure strength of the 90° layer under thermo-mechanical transverse tension is 24 MPa, which is half of the transverse failure strength at room temperature [63] due to the coupled effects of the temperature-dependent material properties and mechanical loading.

The failure mechanisms of the 0° ply in the quasi-isotropic composite under thermo-mechanical loading was more complex than those of the 45° and 90° ply, due to the interplay of fibre breakage and matrix cracking and interface debonding. Fig. 14 shows the progressive failure process of fibre breakage, matrix cracking and interface debonding of the 0° ply. QUADSCRT, DUCTCRT and user-defined variable SDV7 represent the damage to the interface, matrix and fibres, respectively; while the SDEG and SDV9 outputs represent the final failure of the

interface and matrix, and fibres, respectively. It can be seen that early interface debonding was predicted at 50 °C mainly due to the difference in thermal expansion between the interface and fibres and incident mechanical loading. When the temperature reached 100 °C, the RVE reached its maximum stress of 2.5 GPa due to the coupled effects of damage onset within the fibres and matrix cracking. Random fibre breakage was then captured by the RVE model under longitudinal tension when the temperature increased to 175 °C. The final failure of the RVE with fibre breakage, fibre pull-out, matrix cracking and interface debonding were predicted with a comparison of an experimental SEM image of burned CFRP composites shown in Fig. 15 [62].

This trend shows excellent agreement with the experimental data of quasi-isotropic AS4/3501-6 composite laminates, shown in Fig. 10. The specific strength for the composites, shown in orange, is defined as its ultimate failure stress normalised by density. The fitted experimental curve with an R-square value of 0.94 shows that the composite began to lose strength at the glass transition temperature around 100 °C. Carbon fibres within the 0° plies of the composites were able to retain significant strength despite the matrix being fully softened beyond 210 °C and decomposed beyond 350 °C [39]. As such, the failure of the 0° plies of the composite can be the indicator of the final failure of the composite under thermo-mechanical loading.

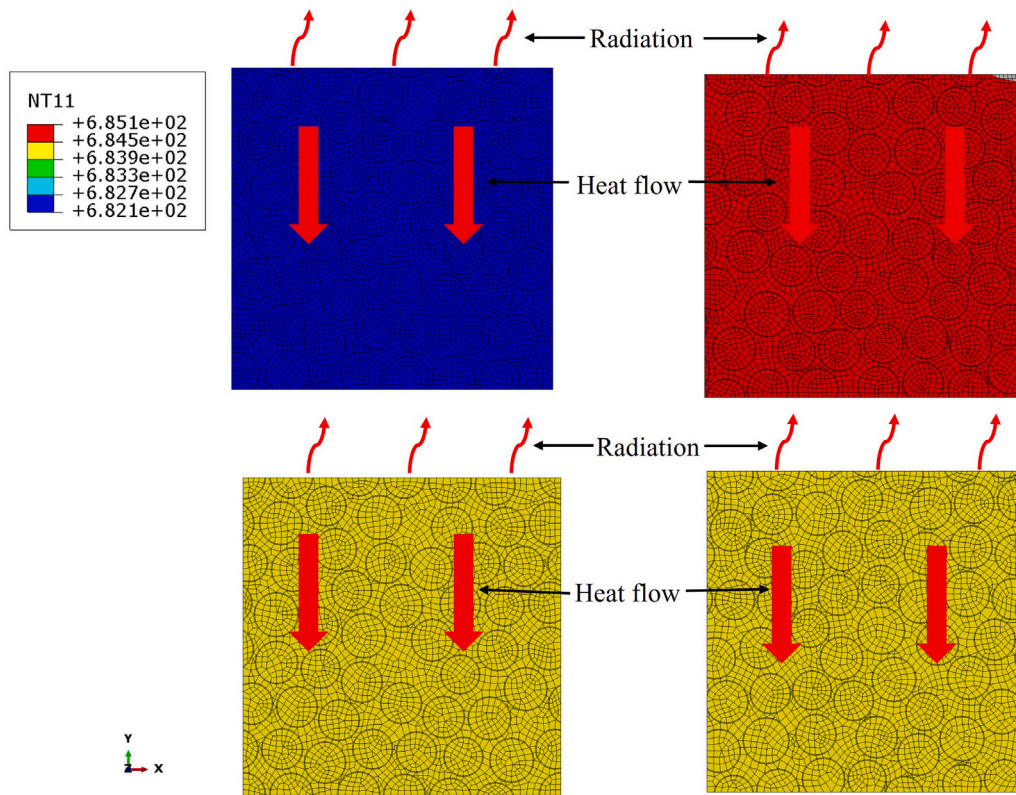


Fig. 9. Node temperature (NT11) field of the RVEs with different fibre distributions at the top layer 45° ply.

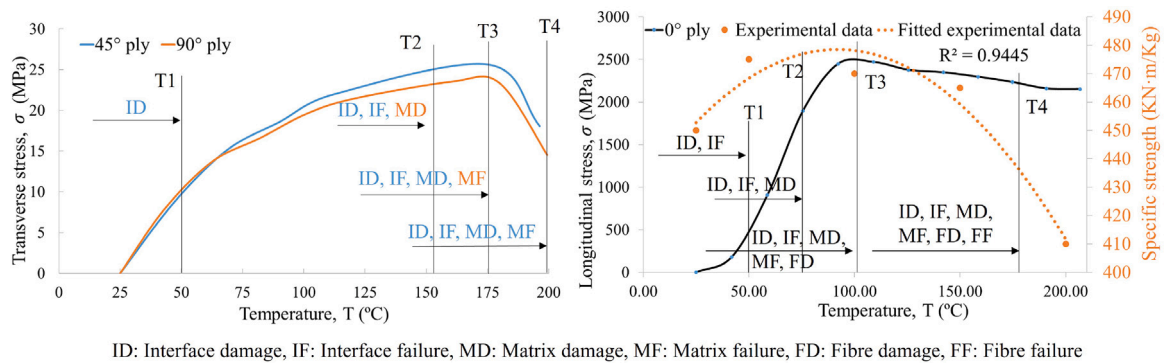


Fig. 10. Stress-temperature curves of 45°, 90° and 0° plies under thermo-mechanical loading.

3.4. Future experimental validation

The work herein has focused on the FE modelling of fire on composite materials under thermo-mechanical loading at both meso- and micro-scales. The mesoscale predicted temperature-time profiles at the front and rear surfaces have been quantitatively validated by the experimental data [39] and the predicted mesoscale composite interlaminar delamination and microscale failure modes of the constituents have been qualitatively validated by the X-ray computed tomography image [39] and SEM images [62]. However, further future experimental validation could enhance the findings and accuracy of the models used. In order to improve the models, particularly at the microscale, a considerable research effort is needed to determine the constituent material behaviour under extreme heating and loading rates. An ad-hoc and carefully designed fixture with heating device could be used with In situ synchrotron computed tomography to investigate the interplay of decomposition of resin and mechanical damage progression for pure resin and CFRP composite. Moreover, push-in and push-out tests based

on aforementioned experiment method could be used to determine the temperature-dependent mechanical properties of fibre/matrix interface. These experiments could significantly improve the understanding of the resin and interface deterioration behaviour and relative offsetting of degradation with heating rate. Thus, the constitutive model of resin and the microscale numerical results could be appropriated quantitatively validated.

4. Conclusions

This work proposed a multiscale sequentially coupled thermo-mechanical modelling framework for the progressive failure analysis of AS4/3501-6 composite material exposed to fire. Firstly, heat transfer was modelled using a mesoscale simulation to predict the temperature profile in the laminate. Thermo-mechanical analysis then characterised the delamination within the laminate at the mesoscale. The heat flux obtained from the mesoscale simulation was then used as an input for the microscale simulations, applied to the top surface of RVE, to predict

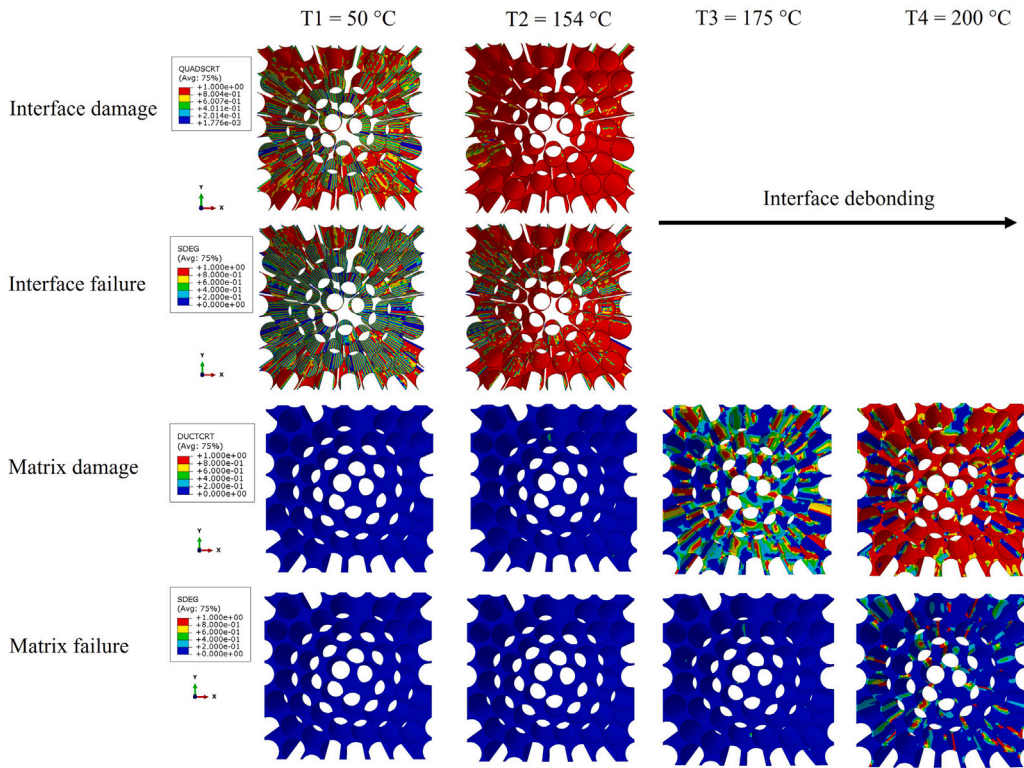


Fig. 11. Progressive failure prediction of matrix and fibre/matrix interface of the top layer 45° ply along with temperature. (The fibres are removed to allow the readers to have a clear view of the damage and failure contours of matrix and fibre/matrix interface inside the RVE in the depth direction.)

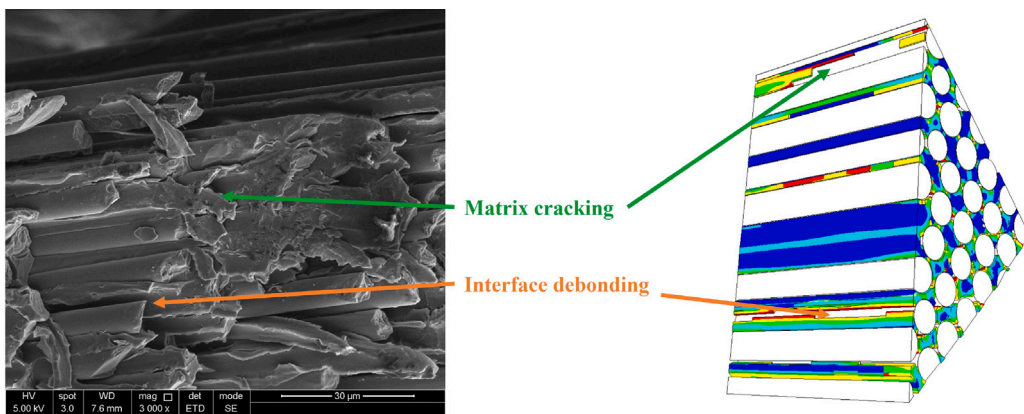


Fig. 12. Predicted matrix cracking and interface debonding in 45° ply compared with the SEM image of burned CFRP composites [62].

the temperature distribution in the RVE. This predicted temperature distribution was then applied as a predefined field for progressive failure analysis of RVEs under thermo-mechanical loading informed by the mesoscale simulation. The main conclusions are listed below.

- Mesoscale simulations could effectively predict the temperature profile through the laminate with good quantitative agreement between predicted and experimental front and rear surface temperatures.
- Temperature predictions at different locations at both the meso- and microscale are in good agreement and the fibre distribution within the RVE model had insignificant influence on the homogenised temperature.
- The multiscale framework was capable of capturing the mesoscale interlaminar delamination and microscale fibre breakage, matrix cracking and interface debonding, with quantitatively and

qualitatively excellent agreements with experimental findings, respectively.

- The laminate can still withstand high tensile loads after the epoxy matrix had undergone glass transition softening, which highlights the significance of the carbon fibres in providing superior mechanical structural performance when exposed to fire.
- The failure of 0° plies within the laminate can be the indicator of specimen final failure under thermo-mechanical loading.

It is worth noting that the modelling strategy in this study is not only capable of simulating the failure of composites under high temperature environment but also at room temperature. The matrix cracking and fibre/matrix interface debonding under transverse tension, and the matrix yielding under transverse compression and in-plane shear were captured at the microscale and the predicted strengths are validated by the experiments with the same modelling approach at room temperature [29,30]. However, it should be mentioned that the results and

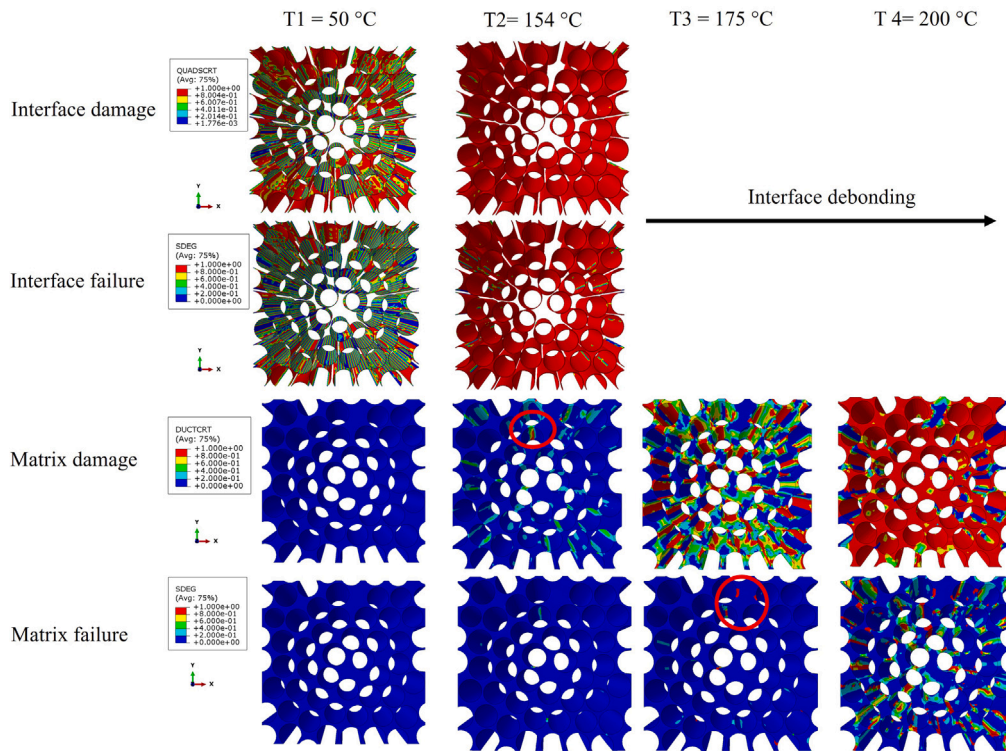


Fig. 13. Progressive failure prediction of matrix and fibre/matrix interface of the 90° ply along with temperature. The fibres are removed to allow the readers to have a clear view of the damage and failure contours of matrix and fibre/matrix interface inside the RVE in the depth direction.

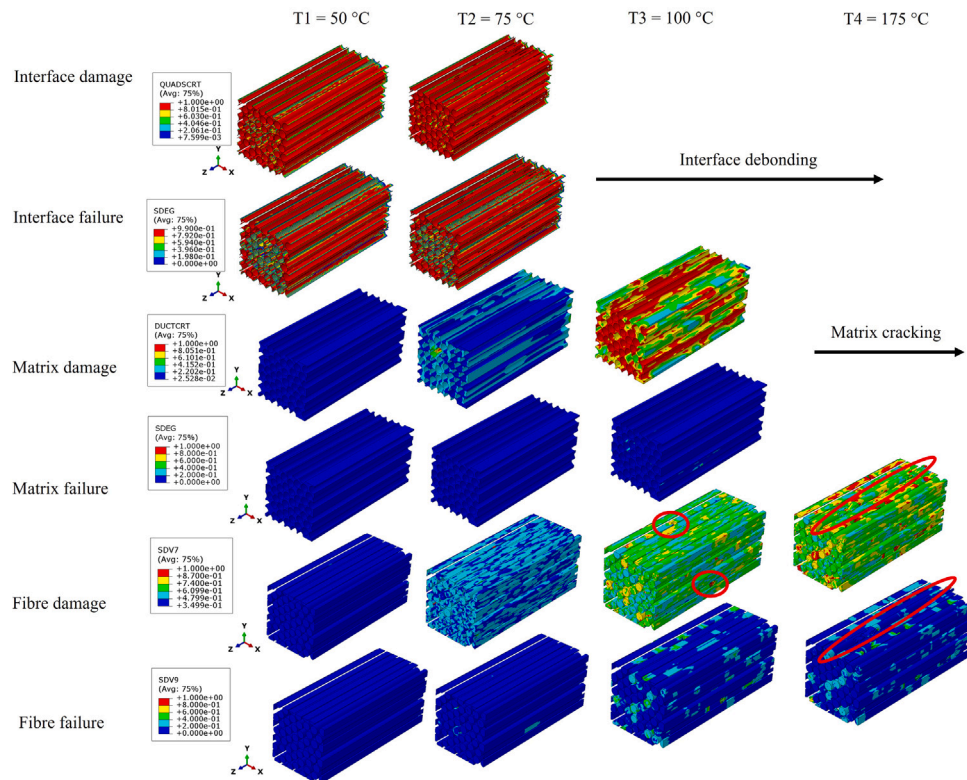


Fig. 14. Progressive failure prediction of the constituents of the 0° ply along with temperature.

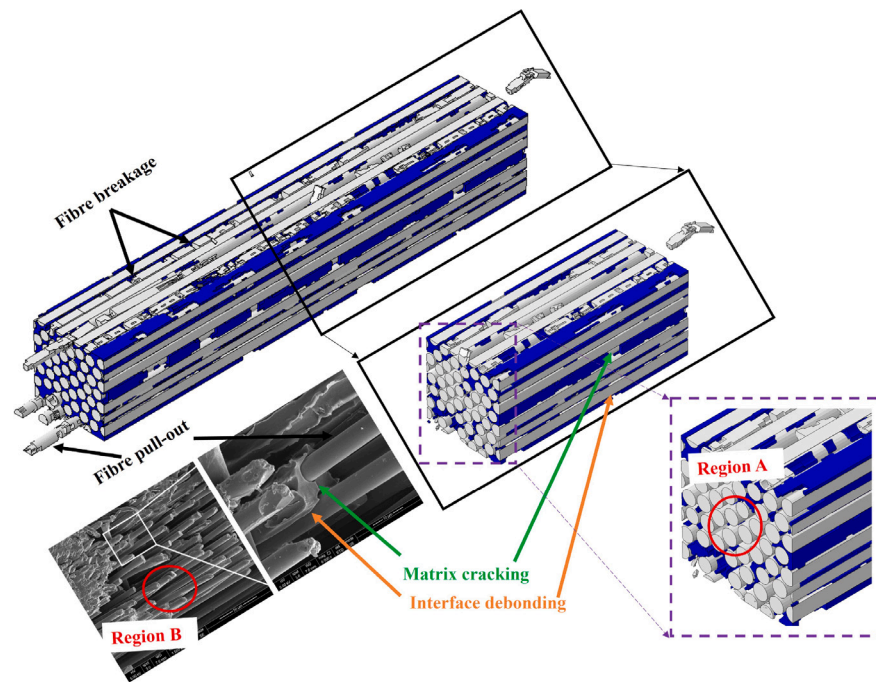


Fig. 15. Predicted matrix cracking and interface debonding in 0° ply compared with the SEM image of burned CFRP composites [62].

findings may only be valid for specific materials and ply configurations because the progressive failure mechanisms may change with different materials and layup sequences. In any case, the framework could be applied to the progressive failure analysis of composite structures with customised needs under thermo-mechanical loading.

CRediT authorship contribution statement

Lei Wan: Writing – review & editing, Writing – original draft, Visualization, Software, Methodology, Investigation, Formal analysis, Data curation, Conceptualization. **Scott L.J. Millen:** Writing – review & editing, Writing – original draft, Methodology, Investigation, Formal analysis, Data curation, Conceptualization.

Declaration of competing interest

The authors declare that they have no known competing financial interests or personal relationships that could have appeared to influence the work reported in this paper.

Data availability

Data will be made available on request.

Acknowledgements

This research did not receive any specific grant from funding agencies in the public, commercial, or not-for-profit sectors. We are grateful for use of the computing resources from the Northern Ireland High Performance Computing (NI-HPC) service funded by EPSRC, United Kingdom (EP/T022175).

References

- [1] Lyu Q, Wang B, Guo Z. Predicting post-impact compression strength of composite laminates under multiple low-velocity impacts. *Composites A* 2023;164:107322.
- [2] Millen S, Xu X, Lee J, Mukhopadhyay S, Wisnom M, Murphy A. Towards a virtual test framework to predict residual compressive strength after lightning strikes. *Composites A* 2023;174:107712.
- [3] Asaro RJ, Lattimer B, Ramroth W. Structural response of FRP composites during fire. *Compos Struct* 2009;87(4):382–93.
- [4] Mouritz A, Feih S, Kandare E, Mathys Z, Gibson A, Des Jardin P, Case S, Lattimer B. Review of fire structural modelling of polymer composites. *Composites A* 2009;40(12):1800–14.
- [5] Sterling J, Tattersall L, Bamber N, De Cola F, Murphy A, Millen S. Composite structure failure analysis post lithium-ion battery fire. *Eng Fail Anal* 2024;160:108163.
- [6] Tewarson A, Macaione D. Polymers and composites - An examination of fire spread and generation of heat and fire products. *J Fire Sci* 1993;11:421–41.
- [7] Mouritz A. Review of smoke toxicity of fiber-polymer composites used in aircraft. *J Aircr* 2009;46:737–45.
- [8] Key C, Lua J. Constituent based analysis of composite materials subjected to fire conditions. *Composites A* 2006;37:1005–14.
- [9] Tranchard P, Samyn F, Duquesne S, Estèbe B, Bourbigot S. Modelling behaviour of a carbon epoxy composite exposed to fire: Part I—Characterisation of thermophysical properties. *Materials* 2017;10(5):494.
- [10] Tranchard P, Samyn F, Duquesne S, Estèbe B, Bourbigot S. Modelling behaviour of a carbon epoxy composite exposed to fire: Part II—comparison with experimental results. *Materials* 2017;10(5):470.
- [11] Nguyen PL, Vu XH, Ferrier E. Elevated temperature behaviour of carbon fibre-reinforced polymer applied by hand lay-up (M-CFRP) under simultaneous thermal and mechanical loadings: Experimental and analytical investigation. *Fire Saf J* 2018;100:103–17.
- [12] Luo C, Lua J, DesJardin PE. Thermo-mechanical damage modeling of polymer matrix sandwich composites in fire. *Composites A* 2012;43(5):814–21.
- [13] Loh TW, Kandare E, Nguyen KT. The effect of thickness on the compression failure of composite laminates in fire. *Compos Struct* 2022;286:115334.
- [14] Feih S, Mouritz A. Tensile properties of carbon fibres and carbon fibre-polymer composites in fire. *Composites A* 2012;43(5):765–72.
- [15] Hulin T, Karatzas V, Mindykowski P, Jomaas G, Berggreen C, Lauridsen D, Dragsted A. Experimental assessment of the robustness in fire of lightweight ship bulkheads. *Mar Struct* 2019;64:161–73.
- [16] Feih S, Mathys Z, Gibson A, Mouritz A. Modelling the tension and compression strengths of polymer laminates in fire. *Compos Sci Technol* 2007;67(3–4):551–64.
- [17] Millen S, Ashworth S, Farrell C, Murphy A. Understanding and representing heating and heating rate effects on composite material properties for lightning strike direct effect simulations. *Composites B* 2022;228:109438.
- [18] Kim J-S, Jeong J-C, Cho SH, Seo S-I. Fire resistance evaluation of a train carbody made of composite material by large scale tests. *Compos Struct* 2008;83(3):295–303.
- [19] Grigoriou K, Mouritz A. Influence of ply stacking pattern on the structural properties of quasi-isotropic carbon-epoxy laminates in fire. *Composites A* 2017;99:113–20.
- [20] Massarwa E, Aboudi J, Haj-Ali R. A multiscale modeling for failure predictions of fiber reinforced composite laminates. *Composites B* 2019;175.

- [21] Kumagai Y, Onodera S, Salviato M, Okabe T. Multiscale analysis and experimental validation of crack initiation in quasi-isotropic laminates. *Int J Solids Struct* 2020;193–194:172–91.
- [22] Sun Q, Meng Z, Zhou G, Lin S-P, Kang H, Keten S, Guo H, Su X. Multi-scale computational analysis of unidirectional carbon fiber reinforced polymer composites under various loading conditions. *Compos Struct* 2018;196:30–43.
- [23] Kawagoe Y, Kawai K, Kumagai Y, Shirasu K, Kikugawa G, Okabe T. Multiscale modeling of process-induced residual deformation on carbon-fiber-reinforced plastic laminate from quantum calculation to laminate scale finite-element analysis. *Mech Mater* 2022;170:104332.
- [24] Watanabe T, Kawagoe Y, Shirasu K, Okabe T. Multiscale model for failure prediction of carbon-fiber-reinforced composites under off-axis load. *Int J Solids Struct* 2023;283:112489.
- [25] Saito R, Yamanaka Y, Matsubara S, Okabe T, Moriguchi S, Terada K. A decoupling scheme for two-scale finite thermoviscoelasticity with thermal and cure-induced deformations. *Internat J Numer Methods Engrg* 2021;122(4):1133–66.
- [26] Tan VBC, Raju K, Lee HP. Direct FE2 for concurrent multilevel modelling of heterogeneous structures. *Comput Methods Appl Mech Engrg* 2020;360:112694.
- [27] Zhi J, Yang B, Li Y, Tay T-E, Tan VBC. Multiscale thermo-mechanical analysis of cure-induced deformation in composite laminates using direct FE2. *Composites A* 2023;173:107704.
- [28] Anjang A, Chevali V, Kandare E, Mouritz A, S. F. Tension modelling and testing of sandwich composites in fire. *Compos Struct* 2014;113:437–45.
- [29] Wan L, Ismail Y, Zhu C, Zhu P, Sheng Y, Liu J, Yang D. Computational micromechanics-based prediction of the failure of unidirectional composite lamina subjected to transverse and in-plane shear stress states. *J Compos Mater* 2020;54(24):3637–54.
- [30] Wan L, Ullah Z, Yang D, Falzon BG. Probability embedded failure prediction of unidirectional composites under biaxial loadings combining machine learning and micromechanical modelling. *Compos Struct* 2023;312:116837.
- [31] Chen J, Wan L, Ismail Y, Hou P, Ye J, Yang D. Micromechanical analysis of UD CFRP composite lamina under multiaxial loading with different loading paths. *Compos Struct* 2021;269:114024.
- [32] Chen J, Wan L, Ismail Y, Ye J, Yang D. A micromechanics and machine learning coupled approach for failure prediction of unidirectional CFRP composites under triaxial loading: A preliminary study. *Compos Struct* 2021;267:113876.
- [33] Chen J, Wan L, Nelms K, Allegri G, Yang D. Failure analysis of unidirectional CFRP composites with the coupled effects of initial fibre waviness and voids under longitudinal compression. *Compos Struct* 2024;118451.
- [34] Totry E, González C, Llorca J. Influence of the loading path on the strength of fiber-reinforced composites subjected to transverse compression and shear. *Int J Solids Struct* 2008;45(6):1663–75.
- [35] González C, Llorca J. Mechanical behavior of unidirectional fiber-reinforced polymers under transverse compression: Microscopic mechanisms and modeling. *Compos Sci Technol* 2007;67(13):2795–806.
- [36] Chen G, Ozden U, Bezold A, Broeckmann C. A statistics based numerical investigation on the prediction of elasto-plastic behavior of WC-Co hard metal. *Comput Mater Sci* 2013;80:96–103.
- [37] Kanit T, N'Guyen F, Forest S, Jeulin D, Reed M, Singleton S. Apparent and effective physical properties of heterogeneous materials: Representativity of samples of two materials from food industry. *Comput Methods Appl Mech Engrg* 2006;195(33–36):3960–82.
- [38] Millen SL, Lee J. Microscale modelling of lightning damage in fibre-reinforced composites. *J Compos Mater* 2023;57(10):1769–89.
- [39] Grigoriou K, Mouritz A. Comparative assessment of the fire structural performance of carbon-epoxy composite and aluminium alloy used in aerospace structures. *Mater Des* 2016;108:699–706.
- [40] Shah S, Lee J. Stochastic lightning damage prediction of carbon/epoxy composites with material uncertainties. *Compos Struct* 2022;282:115014.
- [41] Millen S, Murphy A, Catalanotti G, Abdelal G. Coupled thermal-mechanical progressive damage model with strain and heating rate effects for lightning strike damage assessment. *Appl Compos Mater* 2019;26:1437–59.
- [42] Benzeggagh M, Kenane M. Measurement of mixed-mode delamination fracture toughness of unidirectional glass/epoxy composites with mixed-mode bending apparatus. *Compos Sci Technol* 1996;56(4):439–49.
- [43] Chang F-K, Scott RA, Springer GS. Strength of mechanically fastened composite joints. *J Compos Mater* 1982;16(6):470–94.
- [44] Ismail Y, Yang D, Ye J. Discrete element method for generating random fibre distributions in micromechanical models of fibre reinforced composite laminates. *Composites B* 2016;90:485–92.
- [45] Garoz D, Gilbert F, Sevenois R, Spronk S, Van Paepegem W. Consistent application of periodic boundary conditions in implicit and explicit finite element simulations of damage in composites. *Composites B* 2019;168:254–66.
- [46] Varandas LF, Catalanotti G, Melro AR, Tavares R, Falzon BG. Micromechanical modelling of the longitudinal compressive and tensile failure of unidirectional composites: The effect of fibre misalignment introduced via a stochastic process. *Int J Solids Struct* 2020;203:157–76.
- [47] Tavares RP, Melro AR, Bessa MA, Turon A, Liu WK, Camanho PP. Mechanics of hybrid polymer composites: analytical and computational study. *Comput Mech* 2016;57:405–21.
- [48] Weibull W. A statistical distribution function of wide applicability. *J Appl Mech* 1951.
- [49] Curtin WA. Tensile strength of fiber-reinforced composites: III. Beyond the traditional Weibull model for fiber strengths. *J Compos Mater* 2000;34(15):1301–32.
- [50] Tavares RP, Otero F, Turon A, Camanho PP. Effective simulation of the mechanics of longitudinal tensile failure of unidirectional polymer composites. *Int J Fract* 2017;208:269–85.
- [51] Bažant ZP, Oh BH. Crack band theory for fracture of concrete. *Mat Construct* 1983;16:155–77.
- [52] Yamamoto G, Onodera M, Koizumi K, Watanabe J, Okuda H, Tanaka F, Okabe T. Considering the stress concentration of fiber surfaces in the prediction of the tensile strength of unidirectional carbon fiber-reinforced plastic composites. *Composites A* 2019;121:499–509.
- [53] Swolfs Y, Morton H, Scott AE, Gorbatikh L, Reed PA, Sinclair I, Spearing SM, Verpoest I. Synchrotron radiation computed tomography for experimental validation of a tensile strength model for unidirectional fibre-reinforced composites. *Composites A* 2015;77:106–13.
- [54] Tian T, Cole KD. Anisotropic thermal conductivity measurement of carbon-fiber/epoxy composite materials. *Int J Heat Mass Transfer* 2012;55(23):6530–7.
- [55] Ji X, Matsuo S, Sottos NR, Cahill DG. Anisotropic thermal and electrical conductivities of individual polyacrylonitrile-based carbon fibers. *Carbon* 2022;197:1–9.
- [56] Barbero EJ, Cabrera Barbero J. Damage initiation and evolution during monotonic cooling of laminated composites. *J Compos Mater* 2018;52(30):4151–70.
- [57] Systèmes D. Abaqus documentation. Providence, RI: Dassault Systèmes; 2014.
- [58] Boll D, Bascom W, Weidner J, Murri W. A microscopy study of impact damage of epoxy-matrix carbon-fibre composites. *J Mater Sci* 1986;21:2667–77.
- [59] Naito K, Tanaka Y, Yang J-M, Kagawa Y. Tensile properties of ultrahigh strength PAN-based, ultrahigh modulus pitch-based and high ductility pitch-based carbon fibers. *Carbon* 2008;46(2):189–95.
- [60] HexTow® AS4 carbon fiber datasheet. Hexcel Corporation; 2023.
- [61] Karayaka M, Sehitoğlu H. Failure behavior of unidirectional AS4/3501-6 carbon/epoxy laminates. *J Compos Mater* 1996;30(10):1150–76.
- [62] Li Y, Li R, Lu L, Huang X. Experimental study of damage characteristics of carbon woven fabric/epoxy laminates subjected to lightning strike. *Composites A* 2015;79:164–75.
- [63] Kaddour A, Hinton MJ, Smith PA, Li S. Mechanical properties and details of composite laminates for the test cases used in the third world-wide failure exercise. *J Compos Mater* 2013;47(20–21):2427–42.